NANOSTRUCTURED MAGNESIUM SILICIDE Mg_2Si AND ITS ELECTROCHEMICAL PERFORMANCE AS AN ANODE OF A LITHIUM ION BATTERY

Nazia S. Nazer [1, 2], Roman V. Denys [1], Hanne F. Andersen[1], Lars Arnberg[2], and Volodymyr A. Yartys [1, 2 *]

(1) Institute for Energy Technology, Kjeller, Norway ;(2) NTNU, Trondheim, Norway

ABSTRACT

Nano-crystalline Mg_2Si ($Mg_{67}Si_{33}$) and its Si-rich eutectic ($Mg_{47}Si_{53}$) composition were synthesized by hydrogen desorption-recombination process, casting and rapid solidification techniques. The synthesis of Mg_2Si meets experimental challenges due to a significant difference in the melting temperatures of Mg (650 °C) and Si (1414 °C) and due to easy vaporization of magnesium metal. As cast alloys were obtained by induction melting the precursors, Mg and Si, followed by the casting and water quenching. These alloys were rapidly solidified using a chill block melt spinning which produces ribbons with fine dendritic morphology and a grain size close to 100 nm. Hydrogen desorption-recombination process of MgH_2-Si mixture resulted in a release of ~ 4.67 wt. % H and formation of Mg_2Si. The microstructure of the alloys has been studied using Scanning Electron Microscopy and the relationship between microstructure and electrochemical properties as anodes of the lithium ion batteries was characterised. The electrochemical tests indicate that Si rich eutectic electrode shows a higher charge-discharge capacity than the Mg_2Si intermetallic. Rapidly solidified Mg_2Si and Mg_2Si + Si alloys showed the highest initial discharge capacities of 989 mAh/g and 1283 mAh/g, respectively, superior to the alloys prepared by hydrogen desorption-recombination process and casting. The presence of electrolyte additives FEC (5 %) and VC (1 %) resulted in the formation of the stable SEI layer and enhanced the cycling capacity of the electrodes. Electrochemical Impedance Spectroscopy (EIS) was used to characterize the anode electrodes on cycling. A mathematical model for accounting the impedance response was utilised. The EIS response showed an increased overall resistance for the Mg_2Si eutectic Si-containing alloy electrodes when compared to the electrodes based on a stoichiometric Mg_2Si. Long-term cycling resulted in increased charge transfer resistance, which slowed down the electrochemical processes at the surface of the electrodes.

Keywords:

- Li ion battery
- Mg_2Si anode
- Hydrogen driven synthesis process
- Rapid solidification
- Electrochemical Impedance Spectroscopy

*) Corresponding author. E-mail: volodymyr.yartys@ife.no.

1. INTRODUCTION

Magnesium silicide Mg_2Si, the only intermetallic alloy formed in the Mg-Si system, has several desirable features as a battery anode material for the LIB. These include its high specific electrochemical capacity, low cost of the components, favourable voltage profile and environmental friendliness [1]. Pure Mg_2Si is difficult to prepare by the conventional melting techniques because of a huge difference in the melting points between the Mg (650 °C) and Si (1414 °C). Mechanical alloying (MA) is an alternative approach to solve the aforementioned problems. However, the Mg–Si system cannot be fully transformed into a single phase Mg_2Si by ball milling, as Mg is a ductile metal and during the milling forms a layer deposited at the surface of the vial walls and balls. This results in a low yield of the product and a possible non-homogenous distribution of the elements. In addition, a contamination by such an impurity as Fe is inevitably introduced during a high energy ball milling.

Direct solid phase reaction between MgH_2 and Si is a hydrogen driven chemical route developed to destabilize a rather stable hydride MgH_2 characterised by a strong Mg-H chemical bonding (ΔH = -74 kJ/mol H_2, ΔS = 133 J/mol H_2/K) as a hydrogen storage material [2, 3]. By using MgH_2 and Si, the well crystallized Mg_2Si with 99 % purity and homogenous composition was readily obtained at temperatures below 400 °C. Such a synthesis process provides advantages as compared to the conventional melting technique and MA method allowing overcoming the ductility of Mg and introduction of the impurities.

Paskevicius et al. [4] observed a dehydrogenation of the ball-milled mixture of MgH_2 and Si taking place on heating already to 250 °C, and resulting in the synthesis of the nanocrystalline Mg_2Si with an average crystallite size of 27 nm. The relationship between the synthesis temperature and the structure of Mg_2Si produced by hydrogen driven chemical reaction was investigated in [5] and showed a temperature-dependant grain growth. Indeed, the particle size of Mg_2Si prepared by HDR increased from 500 nm to 2 µm when the synthesis temperature increased from 290 °C to 350 °C. Consistent results were obtained in [1] where Mg_2Si with a diameter of the grains of 1–2 µm was synthesized.

The theoretical electrochemical capacity of Mg_2Si upon electrochemical lithiation is described by the equation $13Li + 4Mg_2Si = 8Mg + Li_{13}Si_4$ [6] which yields 1370 mAh/g and has a favourable voltage profile thus attracting interest to its use as an anode for the Li ion battery. Pena et.al [7] have shown that Mg_2Si delivers a much lower yet quite high initial capacity of about 690 mAh/g. Unfortunately, this value rapidly decreases down to 30 mAh/g already after 25 cycles.

Several studies has been conducted to improve the cyclic stability of Mg-Si system via different methods such as various synthesis techniques which further to the HDR and ball milling also included sputtering [5, 8], variations in the Mg-Si composition ratio [8], pre-insertion of Li [9, 10], and use of carbon composites/carbon coating [11-13].

Mg−Si thin films obtained via combinatorial magnetron sputter deposition with various elemental compositions ranging from $0 \leq x \leq 1$ in $Mg_xSi_{(1-x)}$ were studied in [8]. A maximum electrochemical capacity of 2794 mAh/g (corresponding to 2.8 at. Li per $Mg_{0.26}Si_{0.74}$) was obtained, with capacity retention about 49 % after 400 cycles. The Mg_2Si/C (40% C) composite studied in [13] delivers an initial capacity of 800 mAh/g and has a good cyclic stability (400 mAh/g after 30 cycles).

Kim et al. [14] proposed a three-step mechanism of the electrochemical lithium intercalation into Mg_2Si. After the initial lithium intercalation limit (1 atom of Li/Mg_2Si [14]) was reached, the formed $Li_{critical}Mg_2Si$ decomposed into $Li_{saturated}Mg_2Si$, Mg and Li–Si alloys. At the final stage of the lithiation, the formed Mg reacted with Li to form binary Li–Mg intermetallics.

Alternatively, Moriga et al. [15] reported a two-step lithiation mechanism, which included the formation of a unique ternary phase firstly, Li_2MgSi, and then a formation of Li–Si and Li–Mg binary alloys. Both mechanisms involve an electrochemically driven alloying processes, which because of a presence of elementary silicon result in a poor cyclic performance due to a high volume expansion of Si of about 400 % (when $Li_{22}Si_5$ is formed [16]).

Roberts et al. [17] proposed a three step reaction mechanism, including a limited lithium intercalation into Mg_2Si during the start of the Li insertion process (Step 1), formation of a unique ternary phase, Li_2MgSi together with a binary Li-Si alloy (Step 2), and lithium insertion into magnesium (Step 3), which is leached from Mg_2Si during the reaction Step 2.

The Mg-Si binary phase diagram is shown in Figure 1. There are three solid phases present in this system, including Mg metal (HCP type structure), Si (FCC diamond type stucture) and Mg_2Si intermetallic compound (FCC antifluorite type structure). Some Si can be dissolved in Mg forming a solid solution with HCP type structure, while pure Mg phase does not dissolve in Si. Three invariant equilibria that are identified in this system include: (a) the eutectic equilibrium on the Mg rich side, $L \rightarrow (Mg) + Mg_2Si$ at 637.6 °C, (b) the eutectic equilibrium on the Si rich side, $L \rightarrow (Si) + Mg_2Si$ at 945.6 °C, and (c) crystallisation of Mg_2Si, $L \rightarrow Mg_2Si$, at 1085 °C. The areas of interest of our study (marked by red cycles in Figure 1) include the intermetallic compound Mg_2Si and the Si-rich eutectic region $Mg_{47}Si_{53}$ (Mg_2Si+Si).

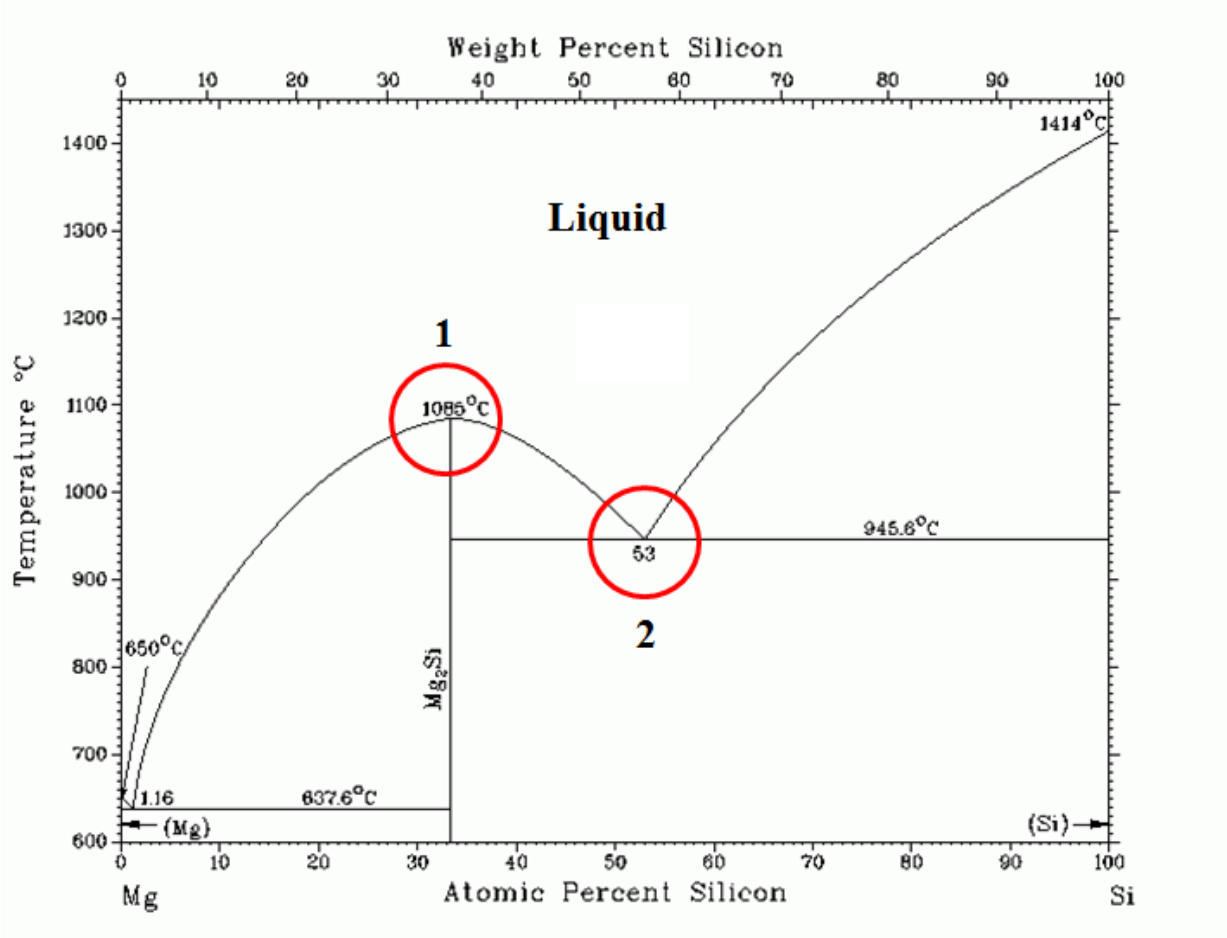

Figure 1. Phase diagram of Mg-Si [18]. The alloys marked by red cycles are (1) Intermetallic compound Mg_2Si ($Mg_{67}Si_{33}$) and (2) Si-rich eutectic $Mg_{47}Si_{53}$ (Mg_2Si+Si) and were used in this study.

The main purpose of the present study was to reveal the relationship between the phase-structural composition and microstructure of the Mg-Si alloys and their electrochemical performance as Li ion battery anodes. The work focuses on the synthesis of Mg_2Si ($Mg_{67}Si_{33}$) and its Si-rich eutectic ($Mg_{47}Si_{53}$) alloys by different methods, including hydrogen driven synthesis, casting and rapid solidification. Based on the study of the capacity failure mechanism of different alloy anodes, we prove that controlling the volume changes [19] and particle size and morphology allows to increase the electrochemical discharge capacity and to improve the cyclic stability.

2. EXPERIMENTAL PROCEDURES

Synthesis of Mg-Si alloy

(a) Hydrogen driven synthesis (HDR)

The stoichiometric Mg_2Si (Mg/Si=2) and Si-rich Mg_2Si eutectic (Mg/Si= 1.78) alloys were synthesized from MgH_2 and Si as starting materials, by applying hydrogen driven desorption-recombination reaction. All materials handling was undertaken in argon filled glove box (impurities not exceeding 0.1 ppm). The MgH_2 (from Acros Organics-95 %) and Si (2 µm average particle size) mixture was loaded into a stainless steel tube reactor which was sealed under an Ar atmosphere. Subsequently, the reactor was placed into a furnace and connected to a Sieverts apparatus to carry out the dehydrogenation by heating to the appropriate temperature allowing a complete hydrogen desorption to occur.

The reactions describing the formation of stoichiometric ($Mg_{67}Si_{33}$) and eutectic Mg-Si ($Mg_{47}Si_{53}$) alloys are presented below:

$$2MgH_2 + Si \rightarrow Mg_2Si + 2H_2 \uparrow \quad (1)$$

$$47MgH_2 + 53Si \rightarrow 23.5Mg_2Si + 29.5Si + 47H_2 \uparrow \quad (2)$$

(b) Casting

The two alloys used in the present study were prepared from the high purity Mg (99 %) and Si (99.98 %). In the casting process, magnesium and silicon were induction melted in a graphite crucible in an electrical resistance furnace protected by a high purity He atmosphere and casted into a steel mould. The molten metal was then cooled by water and allowed to solidify. Extra magnesium (2.5 g per 100 g of Mg) was added in order to compensate for the loss of magnesium due to its easy sublimation during the melting process.

(c) Rapid solidification (RS)

The alloys obtained during the casting process were used as master alloys in the RS process. For the rapid solidification process, the chill block melt spinning method was used. In this method, the master alloy samples were re-melted in a quartz crucible inside a chamber filled with helium and then ejected onto a Cu wheel rotating with a velocity of 1000 rpm, which spun the melt into the thin ribbons (length 25 mm and thickness of 10 µm).

The casted alloys and melt spinned ribbons were then ball milled at 800 rpm for 3 hrs using the SS balls with a diameter 10 mm and a ball to powder ratio 20:1. This resulted in obtaining fine powders which were used to prepare the electrodes.

Characterization

X-ray diffraction measurements of the alloys were conducted using Siemens D5000 X-ray diffractometer with a monochromatic incident beam using the Cu $K_{\alpha 1}$ radiation with the wavelength 1.54056 Å. The powder X-ray data set was collected in the 2θ range from 10° to 140° with a step size of 0.05°. Rietveld refinements for the XRD pattern were carried out using the GSAS [20] suite of programs with the EXPGUI interface [21]. The background of the diffraction pattern was fitted using cosine Fourier function with 6 terms. Background, scale factor, zero point, lattice parameters, atomic positions, and coefficients for the peak shape function were refined in steps until a convergence was achieved.

The morphological features of the alloys were characterized by SEM-Hitachi SU6600 at an accelerating voltage of 10 kV. SEM technique was applied to study the morphology, grain size and phases.

The particle size analysis of the ball milled alloys were done with Malvern Instruments Mastersizer 2000 Particle Size Analyzer with Hydro 2000SM (AWM2002) Dispersion Unit using isopropanol as the dispersing agent.

The working electrode was prepared by mixing 85 % of the active material with 10 % carbon black and 5 % polyvinylidene fluoride (PVDF) dissolved in n-methyl pyrrolidinone (NMP) by ball milling at 300 rpm for 20 minutes. The working electrodes were prepared by tape casting of the slurries on a dendritic Cu foil and dried overnight. The electrodes were further dried at 80 °C in vacuum for 3 hrs. This resulted in a formation of a layer with a thickness of 14 μm. The electrodes were cut into discs (Ø 15 mm) and the mass of the active material was 1.66 mg. Coin type test cells were assembled in Argon filled glove box using Celgard 3401 as a separator, 1M $LiPF_6$ dissolved in EC/PC/DMC (1:1:3) as an electrolyte and Li metal as a counter electrode (380 μm thickness). Electrolyte additives, fluoroethylene carbonate (FEC- 5 %) and vinylene carbonate (VC- 1%), were mixed separately with a solution of EC/PC/DMC (1:1:3) to form the solvent mixtures and the effect of additives was studied.

The electrochemical behaviour of the cells was investigated by cyclic voltammetry (CV) and by galvanostatic measurements at constant current conditions, using an Arbin battery tester within the voltage window 0.02 V-2 V.

Electrochemical impedance spectroscopy (EIS) was performed using a BioLogic SP-300 potentiostat in a frequency range 400 kHz-40 mHz. A small sinusoidal voltage stimulus (10 mV) was applied to an electrochemical cell and its current response was measured. The impedance spectra were fitted to an equivalent circuit using EC Lab software.

XRD analysis of the cycled electrode was carried out using Bruker D8 Advance with Cu Kα radiation at 40 kV and 40 mA. XRD were collected in the 2θ range 10-80 ° with step increments of 0.03 °.

3. RESULTS AND DISCUSSION

3.1 Hydrogen desorption-recombination process

Hydrogen vacuum desorption was performed by linearly heating the MgH_2-Si composite with a rate of 5 °C/min in the temperature range 20-450 °C. Figure 2(a) and Figure 2(b) show the dehydrogenation of stoichiometric mixture $2MgH_2$+Si and of the $47MgH_2$+53Si mixture aimed to result in the formation of Mg_2Si or Mg_2Si+Si eutectic compositions, respectively. The onset of hydrogen desorption was observed at 220 °C, with a sharp peak of hydrogen release at 400 °C. For the mixtures $2MgH_2$+Si and $47MgH_2$+53Si, the total amount of hydrogen released from the composite during the desorption process was ~ 4.67 wt. % and ~ 3.08 wt. %, respectively.

The following chemical reactions takes place between MgH_2 and Si:

Stoichiometric Composition:

$$2MgH_2 + Si \rightarrow Mg_2Si + 2H_2 \uparrow$$

Eutectic Composition:

$$47MgH_2 + 53Si \rightarrow 23.5Mg_2Si + 29.5Si + 47H_2 \uparrow$$

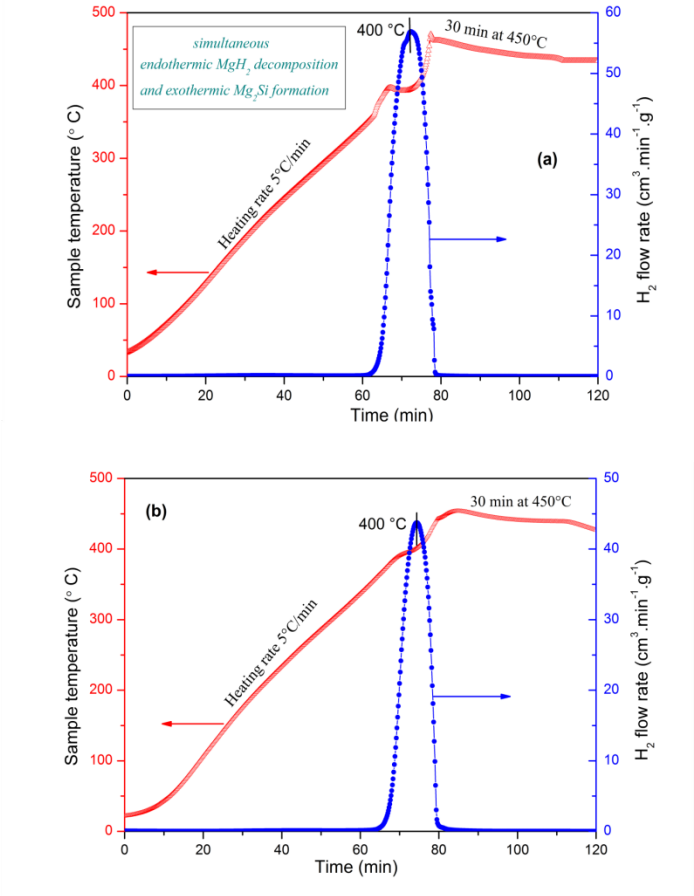

Figure 2. Thermal desorption traces of (a) $2MgH_2$ + Si and (b) $47MgH_2$ + 53Si.

3.2 Microstructure of the Alloys

The resultant powder prepared by the HDR method was identified to be the FCC anti-fluorite-type Mg_2Si (a= 6.352 (1) Å) for the stoichiometric composition and a mixture of Mg_2Si (a= 6.350 (1) Å) and FCC Si (5.424(1) Å) for the eutectic composition. Figure 3 shows the Rietveld refinements of the X-Ray diffraction patterns of the Mg_2Si and its Si rich eutectic alloy prepared by HDR. The absence of any diffraction peaks from MgH_2 and Si in the stoichiometric alloy confirms that the hydrogen desorption was complete and was accompanied by a recombination process.

Rietveld refined XRD pattern of the as-cast Mg_2Si and eutectic alloy are shown in Figure S1 and S2. In case of as-cast eutectic alloy we observed two kinds of crystallographically distinguishable individual Si phases having slightly different lattice parameters - Si1 (a=5.412 (1) Å) and Si2 (a= 5.4313 (4) Å), in addition to the Mg_2Si phase. Table 1 lists the lattice cell parameters and particle size (measured using Particle Size Analyzer after ball milling) for the Mg_2Si and eutectic Mg-Si alloys synthesized by HDR and casting techniques. Phase abundancies of the constituent phases present in the eutectic alloys prepared by HDR and casting are given in Table S1 (see Supplementary Information file. Furthermore, Supplementary Information file contains Figures S1-S14 characterising various aspects of the phase-structural, microstructural and electrochemical characterisation of the studied materials).

Morphology study of the alloys prepared by HDR process (see Figure S3) showed a formation of spherical particles with sizes in the range 1-2 μm.

Morphologies of the as–cast and rapidly solidified Mg_2Si and eutectic alloys are shown in Figure 4. The as–cast Mg_2Si (Figure 4(a)) shows the formation of a homogeneous single phase structure with an average grain size of 50 μm. Such observation well agrees with the XRD analysis data (see Figure S1). The formation of the single phase structure reveals that the amount of the extra added Mg (2.5 %) was sufficient to compensate for the loss of Mg because of evaporation.

The microstructure of the alloy significantly changed after the Rapid Solidification as compared to the as cast sample. The melt spun Mg_2Si ribbons solidified at the chilling surface show a presence of two distinct regions shown in Figure 4(b); large dark Mg_2Si grains have a size of 5-10 μm, while the white intergrain region consists of an eutectic mixture of Mg_2Si and Si. The RS prepared Mg_2Si (see Figure 4(b) and S4) contains be-equiaxed dendritic Mg_2Si, however with a much reduced grain size, down to 1-2 μm in average.

The morphology of the solidifed silicon appears to depend upon the solidification speed, defined by the temperature gradient during the solidification and the local chemical composition, specifically when formed in polyhedral and dendritic forms [22, 23]. As expected, the microstructure of the as-cast eutectic alloy (Figure 4(c)) is very much different as Si becomes a majority component. This microstructure is composed of primary and eutectic Si dispersed in the Mg_2Si matrix (dark grains in Figure 4(c)). For the as-cast eutectic alloy, the presence of two silicon phases – primary (Si1-pure Si) and eutectic (Si2-solid solution of Mg in silicon) is

justified by the Rietveld analysis of the XRD pattern (see Figure S2 and Table 1). Morphology of the Mg_2Si particles (see Figure 4(c) and Figure S5) shows well-distributed round granule grains (dark phase) with an average diameter of 11 µm. As can be seen from Figure 4(c) eutectic silicon shows a dendritic morphology with grain size of appr. 7 µm. In contrast, primary Si particles exhibit a polygonal morphology with a larger grain size, 12-15 µm.

The microstructure of the melt spinned eutectic ribbons produced at 1000 rpm is shown in Figure 4(d). The amount of primary Si decreases considerably and the average grain size is reduced to 1-2 µm. This is due to the high undercooling of the melt spinned alloy during the chill block experiment. Importantly, the primary Si phase is not generated through the remaining nuclei during the soldification. For this reason, the crystallization results in a formation of a small number of primary Si particles. Furthermore, it is clear from Figure 4(d) that the shape and size of the eutectic Si grains is much smaller than those for the as-cast alloy. Very fine and also rather coarse eutectic Si phases are observed in the RS alloy. The dendritic eutectic Si with an average size 100 nm is dispersed in the Mg_2Si matrix (grey regions). The rounded edges of Mg_2Si grains could reduce the possibility of concentration of stresses between the Mg_2Si matrix and the eutectic Si.

Table 1.
Crystallographic data for Mg_2Si and Mg_2Si+Si synthesized by HDR, as-cast alloys and materials obtained by rapid solidification.

Alloys	**Symmetry of the structures and unit cell parameters**		**Particle size (after the ball milling)**		
	HDR	**As-cast**	**HDR**	**As-cast**	**RS**
Mg_2Si	$Fm\bar{3}m$ a= 6.352(1) Å, V=256.278 Å^3	$Fm\bar{3}m$ a= 6.352(1) Å V=256.3 Å^3	1.72 µm	1-10 µm	0.1 -0.6 µm
Mg_2Si +Si	$Fm\bar{3}m$ Mg_2Si, a=6.352 (1) Å, V=256.278 Å^3 $Fd\bar{3}m$ Si, a= 5.424 (1) Å, V=159.598 Å^3	$Fm\bar{3}m$ Mg_2Si, a= 6.35314 (1) Å; V= 259.6 Å^3 $Fd\bar{3}m$ Si1, a= 5.412 (1) Å; V=158.3 Å^3 $Fd\bar{3}m$ Si2, a= 5.4313 (4) Å; V=159.6 Å^3	1.72 µm	1-10 µm	0.1 -0.6 µm

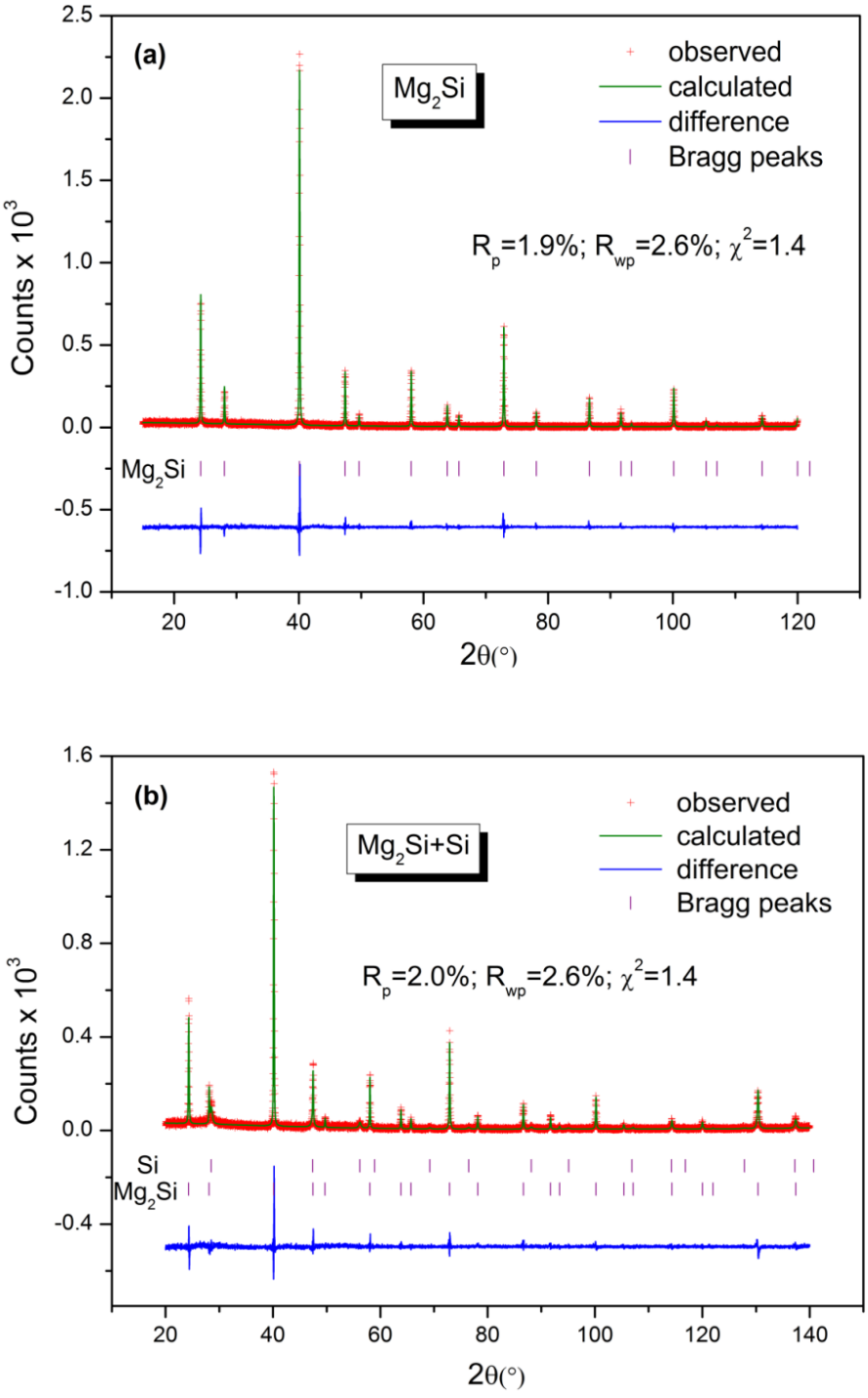

Figure 3. Rietveld refinements of the XRD pattern of (a) Mg_2Si; (b) Mg_2Si +Si, synthesized by HDR method.

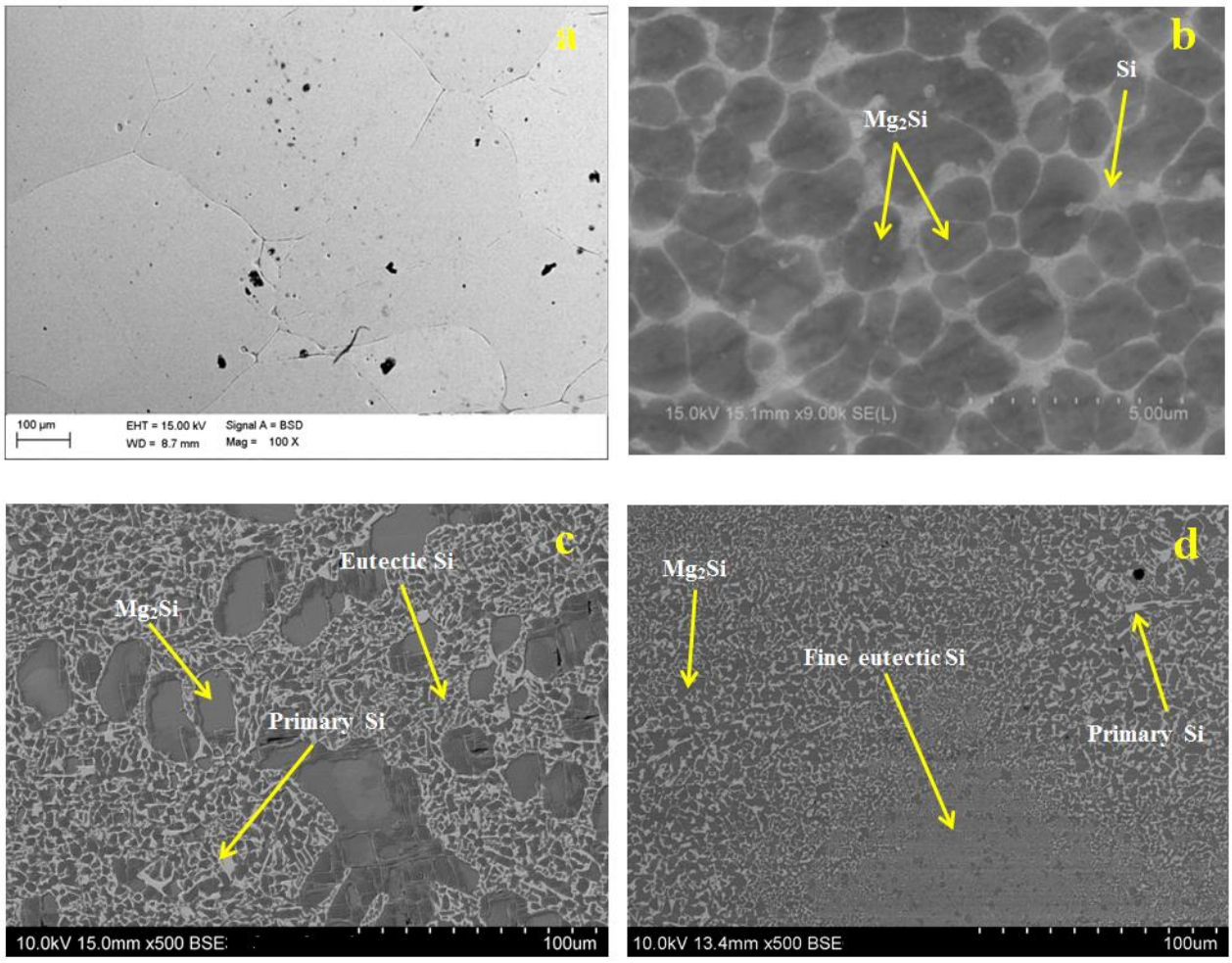

Figure 4. SEM images of Mg-Si alloy ; (a) as cast Mg_2Si; (b) RS Mg_2Si ; (c) as cast Mg_2Si+Si ; (d) RS Mg_2Si+Si.

3.3 Electrochemical studies

3.3.1 Galvanostatic studies

The voltage profiles of the Mg_2Si and eutectic electrodes synthesized by HDR, casting and RS methods were measured in electrolyte with electrolyte additives (1%VC+5%FEC) at a C/20 rate and are shown in Figures 5 (a) and 5 (b), respectively. It is clear that the presence of VC/FEC in the electrolyte solutions increases the discharge capacity for all of the alloys when compared with the voltage profiles for the alloys tested using additive-free electrolyte solution (see Figure S6).

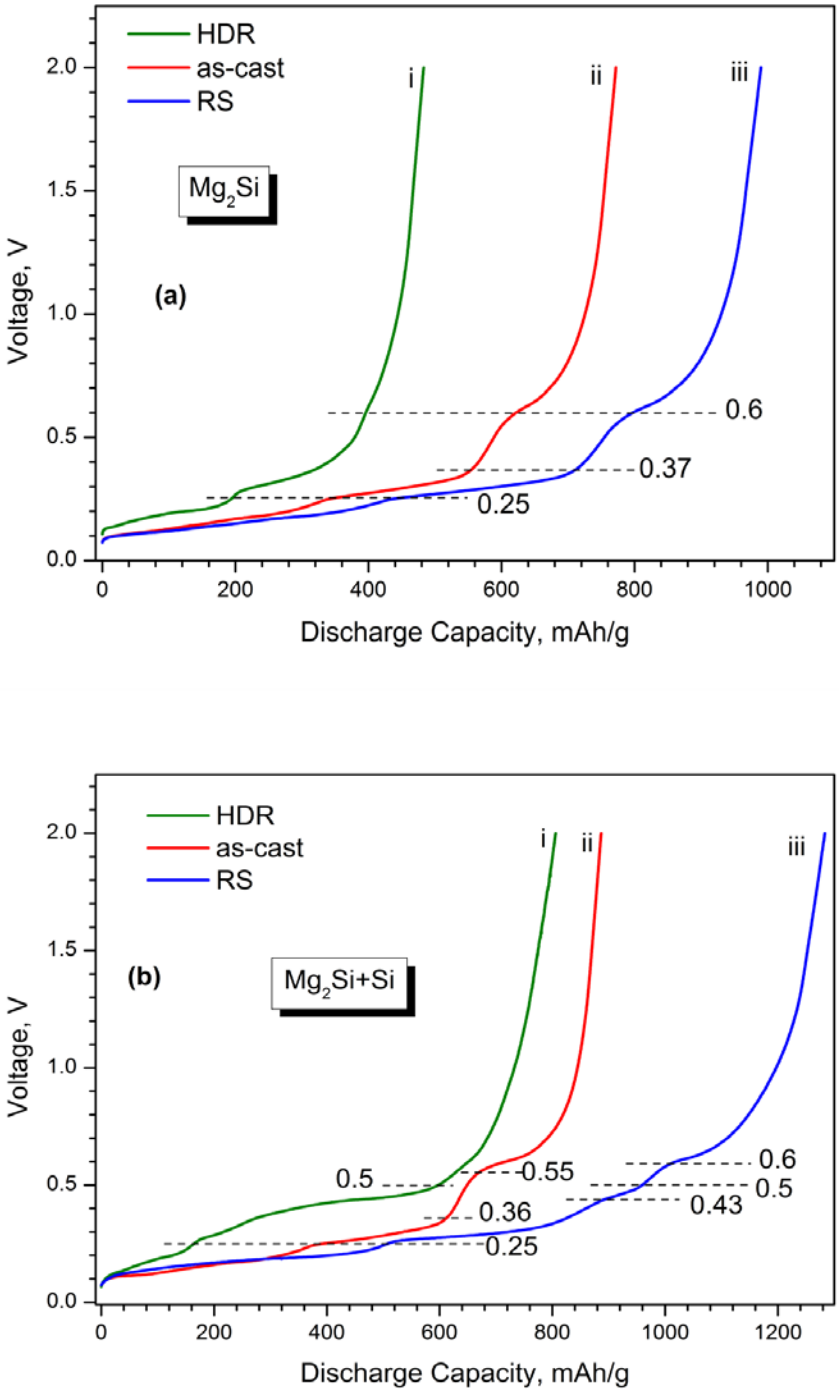

Figure 5. Voltage profiles for (a) Mg_2Si and (b) Mg_2Si+Si electrodes at C/20 rate for the samples synthesized by different routes including (i) HDR; (ii) as-cast and (iii) RS alloys. The data were measured in 1M $LiPF_6$ electrolyte containing EC/PC/DMC (1:1:3)+VC (1 wt.%)+FEC (5 wt.%).

Table 2 shows the data of the initial charge-discharge capacities for the Mg_2Si and Mg_2Si+Si eutectic electrodes synthesized by HDR, as as-cast and as RS alloys. It is clear that rapid solidification results in superior initial reversible capacities (see Figure 5) both for Mg_2Si and for Mg_2Si+Si eutectic, which are as high as 1385 and 1283 mAh/g, respectively. This is significantly higher than the discharge capacities of the HDR alloys (617 and 482 mAh/g, respectively). As the microstructural characterisation showed that the RS alloys have a much smaller grain size as compared to the other studied chemically identical materials, we assume that such an improvement is associated with the advantage of having an improved exchange of lithium during charge and discharge resulting in a superior electrochemical performance.

Table 2. Initial charge/discharge capacities of the Mg_2Si and Mg_2Si+Si eutectic composition prepared by different methods, measured in 1M $LiPF_6$ in EC/PC/DMC (1:1:3) +VC (1 wt.%)+FEC (5 wt.%).

Alloy	**Charge capacity, mAh/g**			**Discharge capacity, mAh/g**		
	HDR	**As-cast**	**RS**	**HDR**	**As-cast**	**RS**
Mg_2Si	617	814	1028	482	771	989
Mg_2Si +Si	869	1073	1808	806	891	1283

Figure 5 shows the presence of a number of distinct electrochemical events indicating that the reaction pathway contains multiple steps. The maximum number of steps is four, but this could decrease to three for some anode materials. As an example, the discharge curve of RS Mg_2Si (Figure 5(a)) exhibits four separate plateaus at 0.02-0.25, 0.25-0.37, 0.37-0.60 and 0.60-2.00 V. In contrast, the discharge curve of the HDR eutectic alloy (Figure 5 (b)) shows just three distinct plateaus at 0.02-0.25 V, 0.25-0.5 V and 0.50-2.00 V because of change of the reaction pathway. Table 3 gives the relation between the voltage plateaus and the discharge capacity exhibited by the alloys. The plateau width in the voltage range 0.25-0.36 V is slightly increased and for the region 0.36-0.60 V, one additional plateau region, 0.50-0.60 V, is formed in case of RS alloy, which is associated with the extra step of delithiation of Si. This extra delithiation event in the case of the RS alloy is responsible for the large delivered discharge capacity.

We note that for the as-cast and RS electrodes, the plateau regions are shifted towards the higher voltages as compared to the materials prepared by HDR. These changes are related to the differences in particle size (see Table 1) and morphology of Mg_2Si and Si, and are in agreement with higher initial capacities of the as cast and RS alloys as compared to the HDR alloys.

Table 3.

Discharge capacities corresponding to the voltage plateaus curves (Fig.5) for the Mg_2Si and eutectic electrode alloys.

				Mg_2Si electrode				
HDR				As-cast		RS		
Voltage Plateau, V	Discharge Capacity, mAh/g	Electrochemical process	Voltage Plateau, V	Discharge Capacity, mAh/g	Electrochemical process	Voltage Plateau, V	Discharge Capacity, mAh/g	Electrochemical process
0.02-0.25	198	$Li_xMg \rightarrow Mg$	0.02-0.25	344	$Li_xMg \rightarrow Mg$	0.02-0.25	437	$Li_xMg \rightarrow Mg$
		$Li_xSi \rightarrow Si$			$Li_xSi \rightarrow Si$			$Li_xSi \rightarrow Si$
0.25-0.60	197	$Li_xSi \rightarrow Si$	0.25-0.37	212	$Li_xSi \rightarrow Si$	0.25-0.37	270	$Li_xSi \rightarrow Si$
0.60-2.00	87	$Li_2MgSi \rightarrow Mg_2Si$	0.37-0.60	69	$Li_xSi \rightarrow Si$	0.37-0.60	84	$Li_xSi \rightarrow Si$
			0.60-2.00	146	$Li_2MgSi \rightarrow Mg_2Si$	0.60-2.00	198	$Li_2MgSi \rightarrow Mg_2Si$
Total capacity	482			771			989	
				Eutectic Electrode				
0.02-0.25	165	$Li_xMg \rightarrow Mg$	0.02-0.25	388	$Li_xMg \rightarrow Mg$	0.02-0.25	508	$Li_xMg \rightarrow Mg$
		$Li_xSi \rightarrow Si$			$Li_xSi \rightarrow Si$			$Li_xSi \rightarrow Si$
0.25-0.50	429	$Li_xSi \rightarrow Si$	0.25-0.36	225	$Li_xSi \rightarrow Si$	0.25-0.43	380	$Li_xSi \rightarrow Si$
0.50-2.00	212	$Li_2MgSi \rightarrow Mg_2Si$	0.36-0.55	59	$Li_xSi \rightarrow Si$	0.43-0.50	72	$Li_xSi \rightarrow Si$
			0.55-2.00	219	$Li_2MgSi \rightarrow Mg_2Si$	0.50-0.60	48	$Li_xSi \rightarrow Si$
						0.60-2.00	275	$Li_2MgSi \rightarrow Mg_2Si$
Total capacity	806			891			1283	

3.3.2 Differential Capacity plots

The electrochemical behaviour of the electrodes studied in the electrolytes with and without the electrolyte additives, VC and FEC, during the Li insertion/removal, has been analysed using the differential capacity plots of the RS samples used as anode electrodes. The data are presented in Figures 6 and S7, respectively.

As the studied anodes operate at low potentials close to 2 V, as characteristic for the metallic lithium, 2.5 V, the reduction of both solvent additives and electrolyte takes place and results in the formation of the solid products forming surface films on the anode surface and creating a solid electrolyte interphase (SEI) layer [24]. The additives of FEC and VC are known to suppress the reduction of solvent and salt, resulting in the formation of thinner and more stable SEI layer films thus lowering the impedance [25]. For the eutectic alloy studied with electrolyte additives, the first lithiation curve shows presence of two weak cathodic peaks at 0.88 V and 1.2 V (Figure 6 (b)). As these peaks disappear after the first cycle, they can be associated with the formation of the SEI layer because of the decomposition of the electrolyte [25, 26].

In contrast, the other five cathodic peaks observed at 0.2, 0.16, 0.13, 0.09 and 0.02 V are present until the 5^{th} cycle, except the peak at 0.16V. With cycling, a new peak at 0.25 V starts to develop. Based on the reference data, we suggest that the cathodic peak at 0.02 V is related to the lithiation of Mg [27], while the peaks at 0.16 and 0.20 V are associated with lithium insertion into Mg_2Si [13]. Finally, the peaks at 0.09, 0.13 and 0.25 V are due to the formation of Li-Si alloys [14, 28, 29].

For the eutectic alloy studied in electrolyte without the additives (Figure S8 (b)), peaks observed at 0.98 and 1.03 V (inset of Figure S8 (b)) correspond to the SEI layer formation. As these peaks are shifting to the higher voltages with cycling, this indicates that further reduction of the electrolyte components EC and DMC is gradually taking place. Note that the SEI layer continues to form in the case of additive free electrode, which explains the reasons for the lowering of the capacity observed for the additive free electrode, whereas in the VC and FEC containing electrolyte eutectic electrode after the first cycle doesn't show any further SEI layer formation.

The formation of these surface films is an important factor responsible for the cycling stability [30]. The addition of VC into the electrolyte increases the stability of the SEI layer. As hydrofluoric acid HF is formed during the reduction of the FEC additive, it can react with the alkali components of the SEI layer to form a more even and LiF-rich surface deposited product [26, 31]. Thus, the processes of exchange of metallic lithium become easier [32]. From the differential capacity plots it is clear that a joint addition of VC and FEC indeed improves the cyclic stability and increases the reversible capacities of the Mg_2Si and eutectic electrode as a result of the HF-caused surface modifications.

For the delithiation process, there are four anodic peaks related to the removal of lithium which are located at 0.19, 0.28, 0.46 and 0.6 V. The peaks at 0.19 and 0.28 V are related to the dealloying of Li-Mg [33] and Li-Si [34] alloys, respectively. At the same time, the deintercalation of lithium from Li_2MgSi is associated with the peak at 0.6 V [14]. An extra anodic peak at 0.4 V develops at the second cycle, which corresponds to the further de-alloying of Si.

One extra anodic peak at 0.46 V is observed in the VC and FEC containing electrolyte as compared to the additive free eutectic electrodes. This additional peak is related to the dealloying of the Li-Si alloys [9, 35] allowing to reach higher capacities for the eutectic alloy in the VC / FEC containing electrolyte.

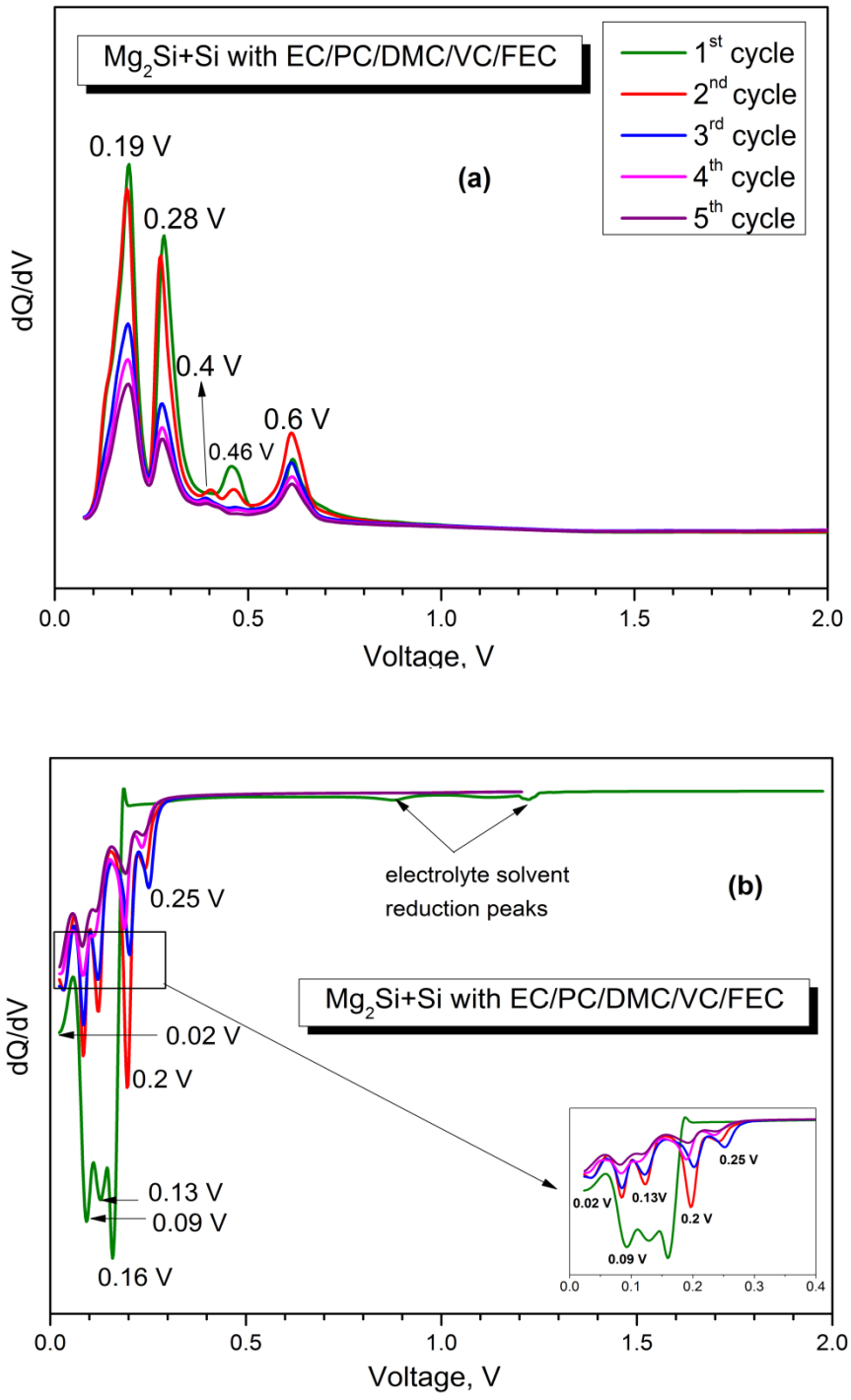

Figure 6. Differential capacity plots for the RS Mg_2Si+Si alloy cycled at 0.05C;
(a) anodic part; (b) cathodic part. Measurements were performed in 1M $LiPF_6$ in EC/PC/DMC (1:1:3) +VC (1 wt.%)+FEC (5 wt.%) electrolyte.

Cyclic voltammetry response of the as-cast Mg_2Si and the Si-rich eutectic alloys was measured in the 1M $LiPF_6$ containing EC/PC/DMC (1:1:3), and is shown in Figure S8 for the first 5 cycles of charge/discharge between 0.02 and 2.00 V versus Li, respectively, at a scan rate of 0.10 mV/s.

For pure as-cast Mg_2Si, CV curves (see Figure S8 (a)) show two cathodic peaks at 0.7 V and 0.15 V in the first scan, which both are related to the formation of solid electrolyte interphase (SEI) film and the lithiation process of Mg_2Si and/or Si, respectively [36, 37]. The observed absence of certain cathodic peaks corresponding to the formation of Li-Si (0.25 and 0.09 V) and Li_2MgSi (0.2V) phases when compared with the differential capacity plot is probably caused by kinetical hindering of the specific reactions [34] when the experimental conditions of the CV measurements are applied.

At the same time, the CV scan of the as-cast eutectic electrode (see Figure S8 (b)) contains only two anodic peaks - centred at 0.35 V and 0.65 V. The peak at 0.35 V should be assigned to the delithiation of the Li-Si alloy and the peak at 0.65 V is attributed to the delithiation event of Li_2MgSi.

The CV scan of Mg_2Si electrode (see Figure S9 (a)) synthesized by HDR shows that, with cycling the anodic peak intensities are increasing which is opposite to the behaviour by the as-cast alloy. This increase in current intensity is due to the cycling induced increase in active surface area of the electrode [25]. Such behaviour could be associated with the spherical morphology characteristic for the HDR alloys. Furthermore, from the CV curves, it is clear that the process has a limited reversibility, which leads to a significant capacity fading.

Even though the anodic CV peak at 0.35 V is quite stable on cycling, we note that this depends on the type of the alloy. Indeed, the anodic peak for the HDR alloy (see Figure S9 (b)) at 0.5 V was initially high and then it weakened upon cycling, suggesting the initial formation and subsequent irreversible delithiation of the Li-Si alloy. This irreversibility is the major reason for the fast capacity fading of the Mg_2Si–Si anode. Thus, the observed large capacities of the eutectic electrode are due to the lithiation of small in size Si particles, leading to the formation of Li_xSi and its subsequent delithiation.

3.3.3 Electrochemical Impedance Spectroscopy

In order to establish the reasons of the capacity fading, the EIS study was performed to analyse the evolution of the electrode/electrolyte interface and focusing on the Mg_2Si and Mg_2Si+Si eutectic alloy prepared by rapid solidification. Cycling dependence of the impedance spectra of the electrodes were recorded at 5^{th}, 10^{th}, 15^{th} cycles from 400 kHz to 40 mHz at 100 % DOD condition at 0.05 C rate.

The EIS Nyquist plot of Mg_2Si and Mg_2Si+Si electrode at different cycles is shown in Figure 7(a) and Figure 7(b), respectively along with the Bode plot. All of the EIS spectra contain a high

frequency semi-circle and a low frequency straight line. As the semi-circle is mainly attributed to the charge-transfer impedance of the electrode/electrolyte interface, thus some information of reactions at the electrode surface can be obtained from the observed changes.

It is clear from the figure that a pronounced difference appears in the semi-circle region for both types of the electrodes. Upon cycling, the circular arc distinctly enlarged, indicating an increased internal resistance. The diameters of the semi-circle for Mg_2Si enlarged from 90 Ω after the 5^{th} cycle to 110 Ω at the 15^{th} cycle, indicating an increase of 22 % in the charge impedance with cycling. The charge impedance of the eutectic electrode showed an increase by 62 % after the 15 cycles. It is interesting that with increase in Si content, the charge transfer resistance became higher with cycling. By contrast, the change in the real part of the impedance for the Mg_2Si electrode with cycling was much less pronounced when compared with the eutectic alloy. This indicates that Mg_2Si electrode provides a much more stable reactive interface between the electrode and electrolyte during the charge-discharge cycling.

In order to validate the fitting of the experimental results obtained during the EIS studies, we have applied a Kramers-Kronig transformation [38-40]. This transformation is valid for a linear, causal, stable and invariant system when the impedance is finite when $\omega \rightarrow 0$ or $\omega \rightarrow \infty$. According to the Kramers-Kronig transformation, the imaginary part of the impedance spectra can be calculated from the real part (or conversely) using the equation [39]:

$$Im\left(Z_{kk}(\omega)\right) = \frac{2\omega}{\pi}\int_0^{\infty} \frac{Re\big(Z(x)\big) - Re\big(Z(\omega)\big)}{x^2 - \omega^2}\, dx$$

Figure S10 shows a good agreement between the experimental (Y) and simulated by using Kramers-Kronig transformation ($Y_{K\text{-}K}$) Bode admittance diagrams for the Mg_2Si electrode after 5 cycles. Thus, the validity of the experimental data was fully confirmed using this transformation.

The EIS data for the Mg_2Si and Mg_2Si+Si electrode can be interpreted with an equivalent circuit shown in Figure S11, where, R_{el} represents the electrolyte resistance between the working and the reference electrode, R_{sei} is the resistance for Li ion conduction in the SEI layer, Q=constant phase element (CPE) represents the space charge capacitance of the SEI layer, R_{ct} represents charge transfer resistance, Q_{ct} represents the double layer capacitance at the electrode surface. The final component W is the Warburg term is proportional to the Li^+ ion diffusion rate into the active electrode material. In the spectra, the semicircle in the high frequency region is attributed to the resistance for Li^+ ion migration into the SEI layer and the medium frequency semicircle relates to the charge transfer resistance (R_{ct}) between the SEI layer and electrode interface and the straight line in the low-frequency region corresponds to the solid-state Li atom diffusion into the active material and insertion capacitance for the accumulation of Li^+ ion in the electrode.

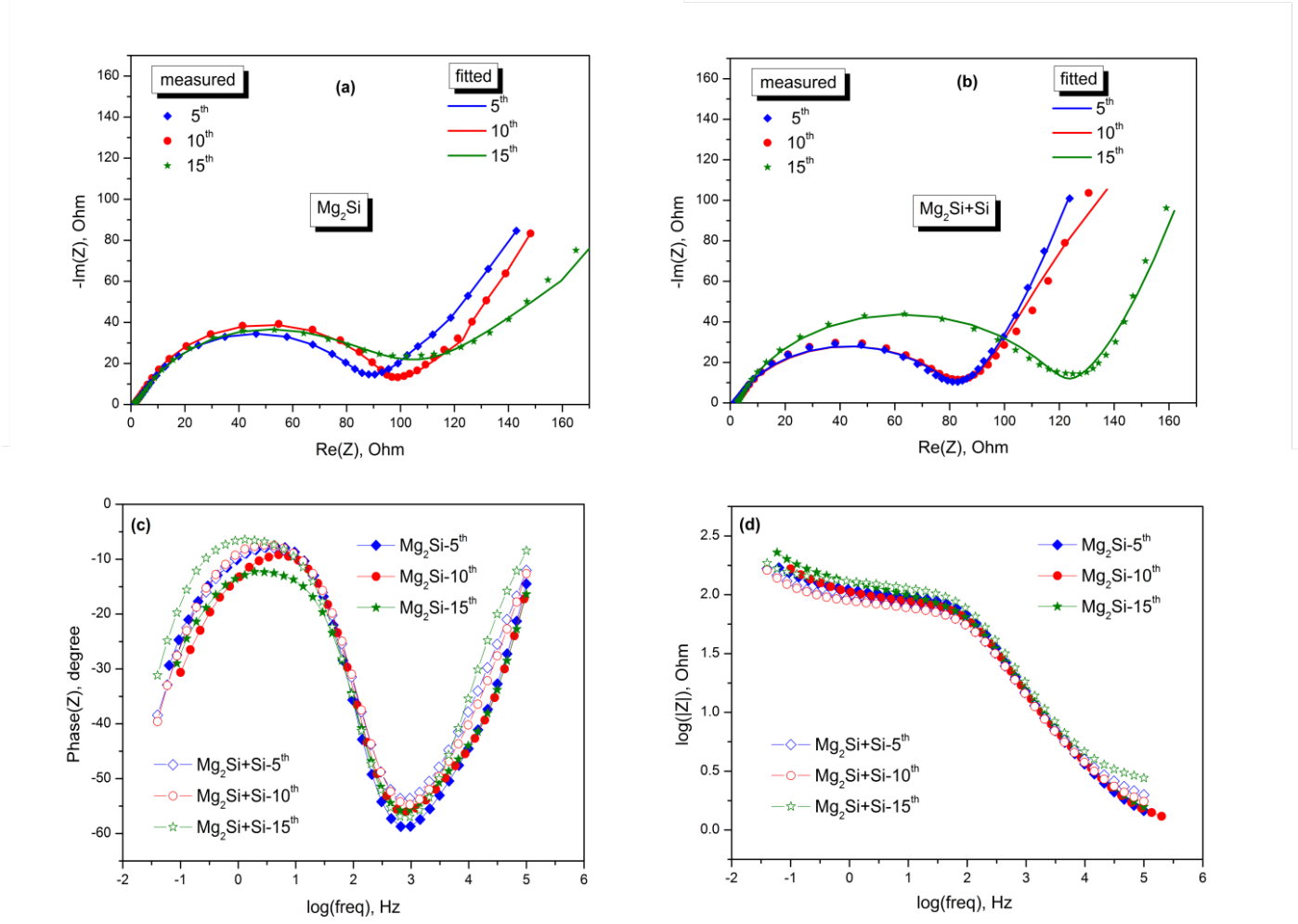

Figure 7. Nyquist plots of Mg_2Si (a) and Mg_2Si +Si (b) electrodes measured in electrolyte without VC and FEC additives measured using Potentiostatic Electrochemical Impedance Spectroscopy (PEIS) technique along with the fitted data after performing different number of cycles at 100 % DOD. E_{WE} = 0 V vs. E_{oc}; V_a = 10 mV; f_{min} = 40 mHz; f_{max} = 400 kHz with 10 points per decade. Bode plots for Mg_2Si and Mg_2Si +Si electrodes; Magnitude (c) and Phase (d).

By fitting the impedance spectra to the equivalent circuit (see Figure S11), the SEI and charge-transfer resistances as a function of cycle number for the Mg_2Si and eutectic electrodes were obtained and are given in Tables 4 and 5, respectively. Both systems exhibit low and stable electrolyte resistance (R_{ele}), with rather small fluctuations. The R_{ct} (see Table 4 and Table 5) values for both the electrodes increases with cycling. This is associated with the dissociation and irreversible lithiation of Mg.

Figure S12 shows comparison of EIS spectra obtained for the Mg_2Si electrode, for the electrolytes with and without the FEC and VC additives. The additive free electrolyte shows a doubled value of the total charge impedance, when compared with the electrolyte with additives. Thus, a lower

charge impedance measured in the VC and FEC containing electrolyte seems to be the reason for the higher capacity shown by the alloy in such a medium.

Table 4.

Fitted parameters of the EIS for the cycled Mg_2Si electrode.

Cycle number Elements and parameters	5	10	15
R1 R_{ele}, Ω	1.314 (2)	1.358 (4)	1.414 (4)
Q1 Q_{sei}, $F.s^{\alpha-1}$ α1*	39 (3) $x10^{-6}$ 0.855 (1)	53 (2) $x10^{-6}$ 0.868 (1)	58 (3) $x10^{-3}$ 0.605 (5)
R2 R_{sei}, Ω	18.77 (3)	21.06 (1)	52.95 (5)
Q2 Q_{ct}, $F.s^{\alpha-1}$ α2*	16 (4) $x10^{-6}$ 0.889 (1)	32 (1) $x10^{-6}$ 0.958 (1)	45 (2) $x10^{-3}$ 0.929 (9)
R3 R_{ct}, Ω	81.9 (1)	88.69 (4)	97.88 (8)
W1 σ, $\Omega s^{-1/2}$	42.51 (6)	56.93 (8)	63.91 (8)
Goodness of fit χ^2	0.0086	0.05	0.0267

Note:
*α1 and α3 are constants which define the slopes of the straight lines in the high frequency and the low frequency positive imaginary part, respectively.

The goodness of the fit (χ^2) is described by the equation [41],

$$\chi 2 = \sum_{i=1}^{n} \frac{|Z_{meas}\ (i) - Z_{model}\ (f_i\ , param)|^2}{{\sigma_i}^2}$$

where,

Z_{meas} (i) - measured impedance at the f_i frequency,
Z_{model} (f_i, param) - function of the chosen model,
f_i is the frequency I,
param - model parameters (ex: R1, R2, Q1, …),
σ_i - standard deviation.

Table 5

Fitted parameters of the EIS for the cycled Mg_2Si+Si electrode.

Cycle number Elements and parameters	5	10	15
R1 R_{ele}, Ω	1.608 (1)	1.64 (4)	2.661(1)
Q1 Q_{sei}, $F.s^{\alpha-1}$ α1*	68 (1) x 10^{-6} 0.849 (1)	59 (2) x10^{-6} 0.845 (1)	49 (2) x10^{-6} 0.810 (5)
R2 R_{sei}, Ω	15.21 (6)	24.84 (2)	67.58 (8)
Q2 Q_{ct}, $F.s^{\alpha-1}$ α1*	49 (1) x 10^{-6} 0.845 (6)	55 (1) x10^{-6} 0.765 (2)	85 (1) x10^{-3} 0.799 (5)
R3 R_{ct}, Ω	71.7 (1)	79.3 (2)	118.2 (6)
W1 σ, $\Omega s^{-1/2}$	19.42 (5)	32.28 (1)	43.37 (5)
Goodness of fit χ^2	0.0094	0.0464	0.0134

3.4 Ex-situ phase-structural analysis of the cycled electrodes

To further understand the lithiation/delithiation mechanism of the Mg_2Si and Mg_2Si-Si eutectic alloys, the electrodes in different lithiation/delithiation states were characterised by XRD studies. The Mg_2Si and eutectic electrodes synthesized by HDR technique were fully lithiated during the charging. The cycled electrodes were washed with dimethyl carbonate (DMC) to remove the remaining electrolyte and then subjected to XRD examination.

Figure 8 shows the Rietveld refinements of the XRD pattern of the cycled eutectic electrode in a fully charged state.

Diffraction peaks of Cu serve as the reference peaks during the refinements of the XRD data with *a*=3.6131(1) Å. In addition to Cu, XRD profiles contain contributions from Li_2MgSi, unreacted Mg_2Si, solid solution of Li in Mg together with residual Si. Interestingly, cubic crystal structures of Mg_2Si and Li_2MgSi are closely related and have very similar values of the unit cell parameters which are close to *a*=6.35 Å for both compounds. This structures similarity leads to the overlap of the entire diffraction peaks characteristic to the FCC lattice of Mg_2Si with the main peaks

characteristic from the primitive unit cell of Li_2MgSi. However, a transformation from the FCC structure of Mg_2Si to the primitive cubic lattice of Li_2MgSi results in the appearance of extra, "superstructure" peaks further to the common for both structures and overlapping peaks. The strongest from these extra peaks appears at $2\theta=31.6^{\circ}$ (hkl = (210)) and is shown in the inset to the Figure 8.

Because of the overlap of the main peaks, the ratio between Mg_2Si and Li_2MgSi can only be found from the Rietveld refinements of the XRD pattern, as a replacement of Mg in Mg_2Si by Li to form Li_2MgSi leads to the change of the intensities of the major peaks. These refinements indicated that the main part of Mg_2Si remained not lithiated with the ratio between Mg_2Si and Li_2MgSi being appr. 4:1. Thus, for the eutectic alloy it is eutectic silicon which mostly contributes to the electrochemical storage capacity of the alloy instead of Mg_2Si itself. Simulated XRD pattern of Mg_2Si and Li_2MgSi is shown in Figure S13. Even though they have similar peaks, the variation in peak intensity and the characteristic peaks of Li_2MgSi confirms its presence in the cycled electrode.

The Rietveld refinement of the XRD pattern of the fully lithiated Mg_2Si electrode is shown in Figure S14. The lithiated Mg_2Si contains only diffraction peaks from the solid solution of Li in Mg_2Si, $Li_{0.27}Mg_{1.96}Si$. We note that the formation of the Li-Si alloy was not confirmed by the XRD data probably due to the amorphization of Si during the lithiation.

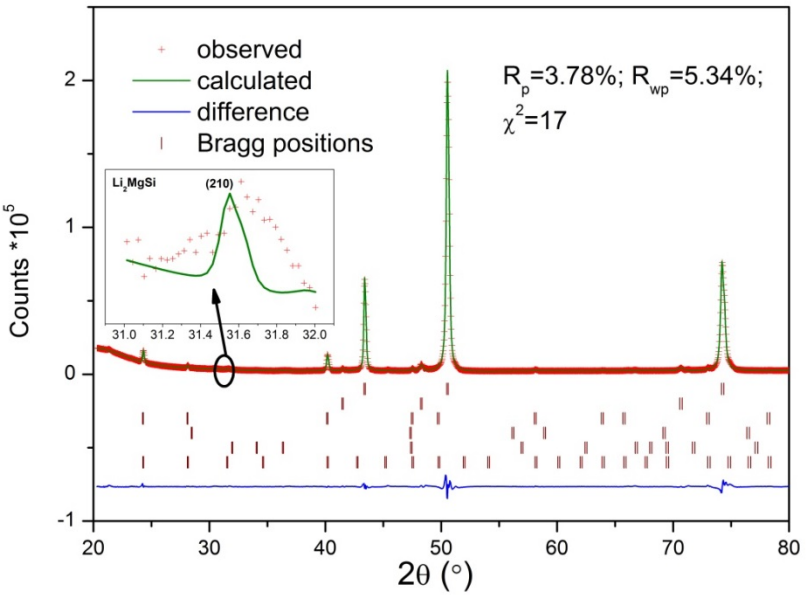

Figure 8. Rietveld refinement of the XRD pattern of a fully lithiated Mg_2Si+Si electrode. Bragg peaks positions for the contributing phases are shown (from top to bottom) for Cu, Fe, Mg_2Si, Si, Li_xMg and Li_2MgSi. Inset plot shows the peak at $2\theta=31.6^{\circ}$ (210), the only observed peak of Li_2MgSi not overlapping with Mg_2Si.

Crystallographic characteristics of the constituent phases and their abundances obtained from Rietveld refinement of the ex-situ XRD data for the fully lithiated Mg_2Si and eutectic electrode are given in Tables 6 and 7, respectively.

By jointly considering the CV, dQ/dV and XRD data, the mechanism of lithium insertion into the Mg_2Si electrode can be described as follows:

$(x+y)Li^+ + (x+y)e^- + Mg_2Si \rightarrow Li_xMg_2Si + Li_ySi + Mg$ …… (Step 1)

$xLi^+ + xe^- + Mg \rightarrow Li_xMg$……..…….. (Step 2)

To summarize the processes during the lithium insertion into the Mg_2Si+Si electrode:

$xLi^+ + xe^- + Si \rightarrow Li_xSi$ ……. (Step 1)

$2Li^+ + 2\,e^- + Mg_2Si \rightarrow Li_2MgSi + Mg$ …….. (Step 2)

$xLi^+ + xe^- + Mg \rightarrow Li_xMg$…… (Step 3)

Schematically, the reaction steps during the lithiation and delithiation of the eutectic and stoichiometric electrodes are shown below in Figure 9 .

The reaction mechanism for the eutectic alloy allows pointing out the reason for its higher discharge capacity when compared with stoichiometric Mg_2Si. This is the lithiation of Si to form Li_xSi for the eutectic Mg_2Si+Si alloy. The reason that Mg_2Si did not entirely disappear in the fully lithiated state in the eutectic alloy is that the reaction steps 3 and 2 overlap.

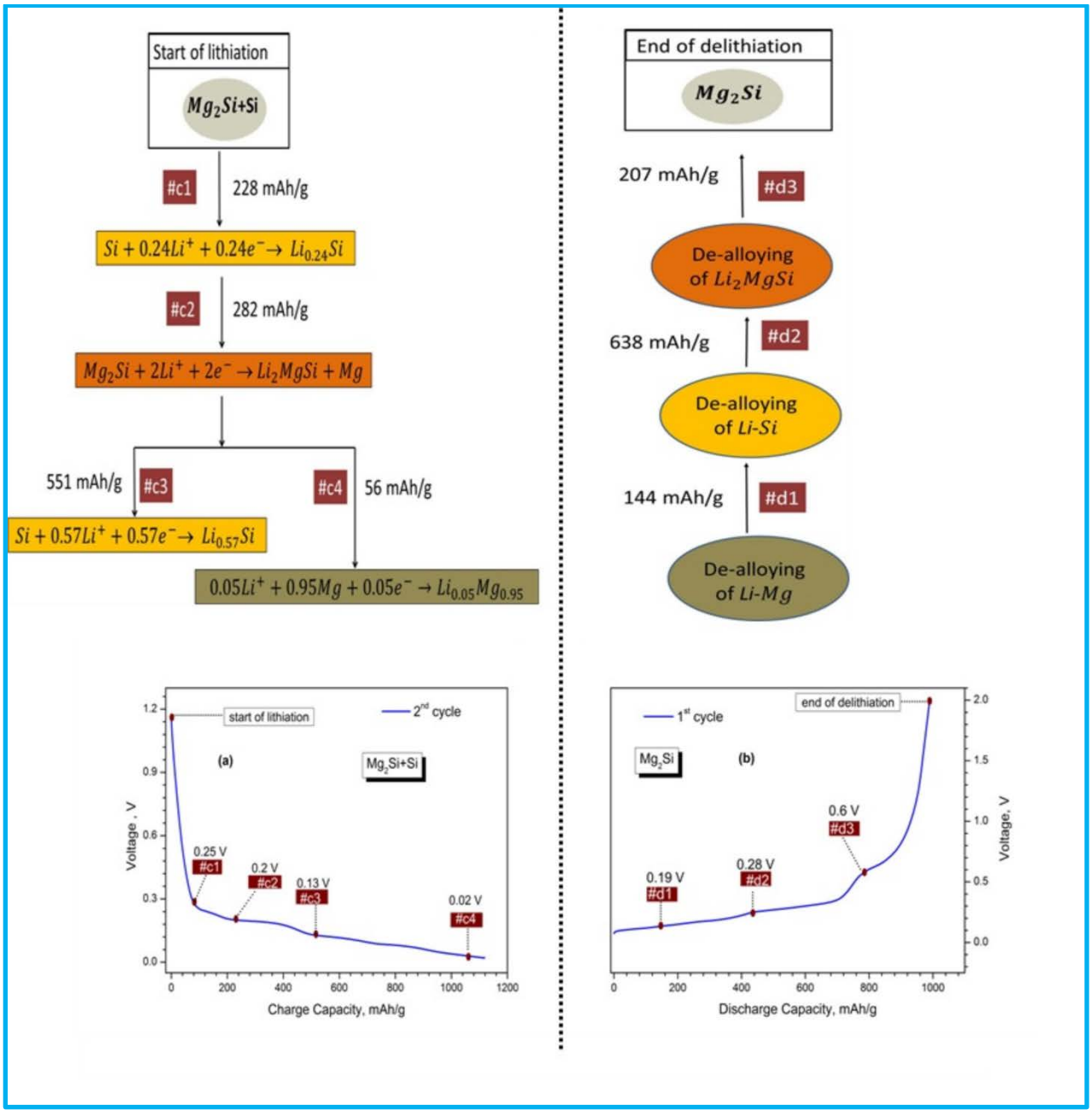

Figure 9. Schematic diagrams of phase transformations for the eutectic electrode on lithiation (a) and for the Mg_2Si electrode on de-lithiation (b). The diagrams show schematically the progression of various steps during galvanostatic tests at C/20. The left scheme assumes presence of four lithiation processes taking place for the Mg_2Si+Si eutectic alloy. The mechanism of the discharge for the stoichiometric Mg_2Si alloy is presented on the right and assumes three de-lithiation events.

The crystal structures of Mg_2Si and its corresponding lithiated derivatives which could be potentially formed during the charging of the anode were all used in the refinements of the XRD data and are presented in Figure 10.

Initial intermetallic alloy Mg_2Si crystallizes in the antifluorite type structure with space group $Fm\bar{3}m$. The Si atoms form a FCC sub lattice with a lattice constant a and the Mg atoms form a simple cubic sublattice with lattice constant a/2. Si atoms are situated in the centres of the cubes created by Mg atoms, whereas Mg atoms are tetrahedrally coordinated by Si atoms.

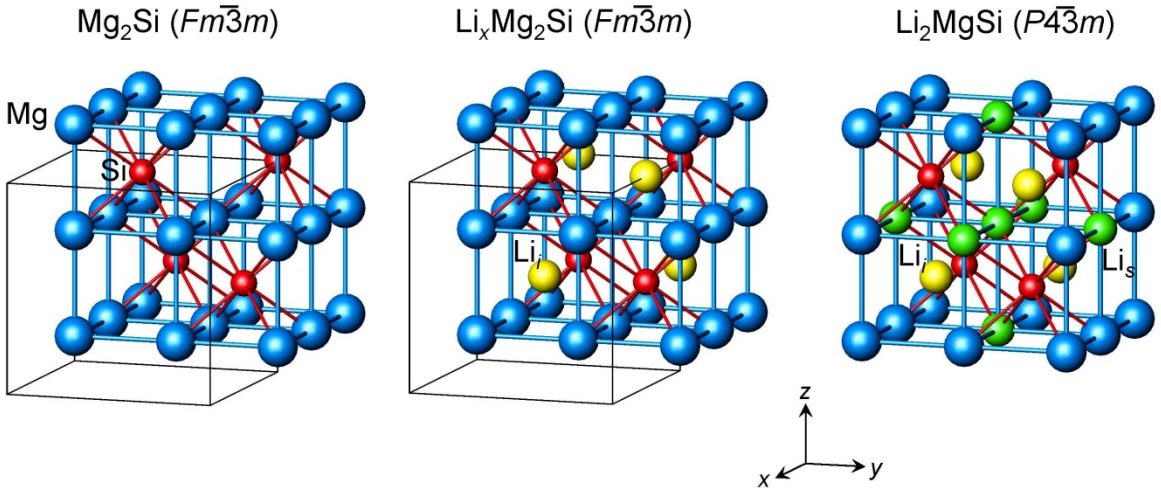

Figure 10. Crystal structures of Mg_2Si and its lithiated derivatives $LiMg_2Si$ and Li_2MgSi.

On interaction with lithium, Mg_2Si first dissolves lithium to form an interstitial solid solution Li_xMg_2Si. This solid solution is formed by insertion of Li into the Mg_8 cubes (see Figure 10; Li atoms are idenfied as Li_i – from Li insertion mechanism) [42]. Ineratomic distance Li-Mg equals 2.75 Å and is significantly shorter than the sum of the atomic radii ($r_{Mg}+r_{Li}$=1.60+1.56=3.16 Å). Even though a maximum lithium content could be as high as x ~ 0.91 [43], practically reached in our work limit was lower, around 0.27 at.Li/f.u.Mg_2Si.

Further Li insertion into Mg_2Si results in the formation of Li_2MgSi and leads to a corresponding simultaneous "leaching" of Mg; its atoms become substituted by Li atoms. These Li atoms are identified as Li_s in Fig. 10 (from substituting). Three different types of crystal structures were reported for Li_2MgSi in the reference data, all with cubic symmetry. An FCC structure with $F4\bar{3}m$ symmetry was observed in an experimental study of the Li–(Si, Mg)–Al phase diagram [44], while two other possible structural models – crystallising with $P4\bar{3}m$ and $Fm\bar{3}m$ space groups – were suggested for Li_2MgSi based on the data of the theoretical simulations [45].

The lithiated phase of Mg_2Si observed in present study during studies of the eutectic alloy fits well with the Li_2MgSi model reported in [46] and the corresponding refined crystallographic data

is given in Table 8. The shortest Li-Li interatomic distances in the structure are Li_i-Li_s of 2.75 Å (2 r_{Li}=3.12 Å) and suggest a possibility of easy Li diffusion along the chains …Li_i-Li_s-Li_i-Li_s… in case of the vacancies on the Li_i sites, which is indeed the case.

Table 6

Crystallographic characteristics of the constituent phases for the fully lithiated Mg_2Si electrode obtained from Rietveld refinement of ex-situ X-ray diffraction data.

Phase	**Space Group**	**Unit cell parameters**	
		Fresh electrode	Fully lithiated
Mg_2Si	$Fm\bar{3}m$	a=6.3487(1) Å V=256.28 (5) Å^3	-
$Li_{0.27}Mg_{1.96}Si$	$Fm\bar{3}m$	-	*a* = 6.3499(2) Å V=260.67(6) Å^3

Table 7

Crystallographic characteristics of the constituent phases for the fully lithiated eutectic electrode obtained from Rietveld refinement of ex-situ X-Ray diffraction data.

Phase	**Space Group**	**Unit cell parameters**	
		Fresh electrode	Fully lithiated
Mg_2Si	$Fm\bar{3}m$	a = 6.3541(3) Å V= 256.54 (3) Å^3	a= 6.3518(5) Å V= 256.27(6) Å^3
Si	$Fd\bar{3}m$	*a*= 5.431(3) Å V= 160.23(5) Å^3	a =5.431(–) Å V=160.23 Å^3
$Li_{0.05}Mg_{0.95}$	$P6_3/mmc$	-	*a*=3.234(6), *c*= 5.26(2) Å V=47.67(5) Å^3
Li_2MgSi	$P4\bar{3}m$	-	6.345(1) Å V=255.5(2)Å^3

Table 8

Crystal structure data for the identified phase constituents

Phase	**Space group, atoms, types of sites and atomic coordinates**	**Type of Li atoms**	**Occupancy**
Mg_2Si	$Fm\bar{3}m$ Mg in 8*c* (¼,¼,¼) Si in 4*a* (0, 0, 0)		 1 1
$Li_{0.27}Mg_{1.96}Si$	$Fm\bar{3}m$ Li1 in 8*c* (¼,¼,¼) Li2 in 4*b* (½,½,½) Mg in 8*c* (¼,¼,¼) Si in 4*a* (0, 0, 0)	 Li_s Li_i	 0.021 (6) 0.232 (2) 0.979 (6) 1
Li_2MgSi	$P4\bar{3}m$ Li1 in 3*c* (0, ½,½) Li2 in 1*b* (½,½,½) Li3 in 4*e* (0.68,0.68,0.68)* Mg in 1*a* (0,0,0) Mg in 3*d* (½,0,0) Si in 4*c* (0.25, 0.25, 0.25)*	 Li_s Li_i Li_s	 1 1 1 1 1 1
$Li_{0.05}Mg_{0.95}$	$P6_3/mmc$ Mg in 2*c* (0.333,0.666, ¼) Li in 2*c* (0.333,0.666, ¼)	 Li_s	 0.95** 0.05

*Li and Si positions are refined using the values Li in 4*e* (0.727,0.727, 0.727) and Si (0.253,0.253,0.253) taken from [46].

**Occupancy estimated based on the electrochemical data.

Finally, it should be noted that because of the very similar crystallographic data for Mg_2Si, Li_xMg_2Si and Li_2MgSi and a very limited accuracy of X-Ray diffraction to determine lithium content in the studied materials, all transformations where these phases appear to be in equilibrium should be preferably characterised by neutron scattering which will provide the data on the distribution of Li between the phases and on the atomic structures of the studied materials.

Thus, the data on the abundancies of the phases presented in Tables 6 and 7 should be considered as having qualitative rather than quantitative character.

4. CONCLUSIONS

In this paper, we demonstrated that pure nano-crystalline Mg_2Si and Si rich Mg_2Si-Si eutectic alloy can be synthesized via the hydride desorption-recombination route, casting and rapid solidification resulting in a significant change in particle size ranging between 1.72 μm (HDR), 1 μm (as cast) and 0.1 μm/100 nm (RS). Morphology studies of the as-cast and rapidly solidified eutectic alloys show the formation of a mixture of primary (polygonal morphology) and eutectic (dendritic) silicon in the Si rich eutectic alloy.

Mg_2Si and its Si rich eutectic have been investigated as anode materials for the rechargeable lithium ion batteries and these studies revealed the effect of grain size and morphology of the constituent phases on their electrochemical performance. The highest maximum discharge capacity of the pure Mg_2Si and Mg_2Si-Si eutectic (respectively, 989 and 1283 mAh/g) were obtained for the Rapidly Solidified alloys. Their performance was superior to the alloys prepared by casting and via hydrogen driven route, and these superior characteristics are associated with a significantly smaller grain size of the phase constituents in the RS alloys allowing faster and easier lithium exchange on cycling.

The differential capacity plot and CV analysis show that in both the alloys the lithiation has a multistep mechanism. This reaction mechanism includes: (a) lithium insertion into the Mg_2Si, followed by (b) the leaching of Mg and its partial substitution by lithium and alloying of silicon and lithium and (c) consecutive lithiation of Mg in the follow-up electrochemical step. Lithiation of Si results in reaching a significant Li/Si ratio of 0.81 and leads to the formation of amorphous lithiated silicon products.

The presence of FEC and VC additives in the electrolyte solutions significantly enhances the initial capacity of the electrodes. From the CV analysis we conclude that a stable SEI layer is formed in the additive-based electrolytes, resulting in higher electrochemical capacities.

Based on the EIS data we observe that Mg_2Si anode material has a lower charge-transfer resistance and forms a stable reactive interface surface layer. In contrast, the eutectic electrode exhibits much higher charge impedance which increases with cycling as compared to the Mg_2Si anode, due to the contribution from elementary Si. Thus, the Mg_2Si electrode provides a significantly more stable reactive interface between the electrode and electrolyte during the charge-discharge cycles. Importantly, EIS analysis revealed a beneficial effect of FEC and VC additions, which allow reducing the total charge impedance of the Mg_2Si electrode.

XRD results showed that the resulting product is $Li_{0.27}Mg_{1.96}Si$ when the Mg_2Si electrode is charged to 1 cycle, whereas the eutectic alloy contains $Li_{0.05}Mg$ alloy and Li_2MgSi as the final lithiation product. Further studies should be done to improve the cycle stability of the Mg-Si alloys and battery anodes of the LIB and to achieve their satisfactory performance at high current densities.

Supplementary data related to this article can be found at http://10.1016/j.jallcom.2017.XXXX

ACKNOWLEDGEMENTS

This work was supported by Research Council of Norway and the European Spallation Source [grant number 234246].

REFERENCES

[1] Y. Liu, Y. He, R. Ma, M. Gao, H. Pan, Improved lithium storage properties of Mg_2Si anode material synthesized by hydrogen-driven chemical reaction, Electrochem. Commun., 25 (2012) 15-18.
[2] J. J. Vajo, F. Mertens, C. C. Ahn , R.C. Bowman Jr, B. Fultz, Altering Hydrogen Storage Properties by Hydride Destabilization through Alloy Formation: LiH and MgH_2 Destabilized with Si, J.Phys.Chem.B, 108 (2004) 13977-13983.
[3] A-L.Chaudhary, M.Paskevicius, D. A. Sheppard, C.E. Buckley, Thermodynamic destabilisation of MgH_2 and $NaMgH_3$ using Group IV elements Si, Ge or Sn, J.Alloys Compd., 623 (2015) 109-116.
[4] M. Paskevicius, D.A. Sheppard, A.L. Chaudhary, C.J. Webb, E.M.A. Gray, H.Y. Tian, V.K. Peterson, C.E. Buckley, Kinetic limitations in the Mg–Si–H system, Int. J. Hydrogen Energy, 36 (2011) 10779-10786.
[5] Y. He, Y. Liu, R. Ma, M. Gao, H. Pan, Synthesis temperature dependence of the structural and electrochemical properties of Mg_2Si anodic materials prepared via a hydrogen-driven chemical reaction, Ionics, 21 (2015) 2439-2445.
[6] A. Anani, R. A. Huggins, Multinary alloy electrodes for solid state batteries I. A phase diagram approach for the selection and storage properties determination of candidate electrode materials, J. Power Sources, 38 (1992) 351-362.
[7] J. Santos-Peña, T. Brousse, D.M. Schleich, Mg_2Si and MSi_2 (M=Ca, Fe) silicon alloys as possible anodes for lithium batteries, Ionics 6(2000) 133.
[8] G. Schmuelling, M. Winter, T. Placke, Investigating the Mg-Si Binary System via Combinatorial Sputter Deposition As High Energy Density Anodes for Lithium-Ion Batteries, ACS Appl. Mater. Interfaces, 7 (2015) 20124-20133.
[9] R. Ma, Y. Liu, Y. He, M. Gao, H. Pan, Chemical Preinsertion of Lithium: An Approach to Improve the Intrinsic Capacity Retention of Bulk Si Anodes for Li-ion Batteries, J. Phys. Chem. Lett., 3 (2012) 3555-3558.
[10] R. Ma, Y. Liu, Y. Yang, K. Pu, M. Gao, H. Pan, Li–Si-alloy-assisted improvement in the intrinsic cyclability of Mg_2Si as an anode material for Li-ion batteries, Acta Mater., 98 (2015) 128-134.
[11] C. Xiao, N. Du, H. Zhang, D. Yang, Improved cyclic stability of Mg_2Si by direct carbon coating as anode materials for lithium-ion batteries, J. Alloys Compd., 587 (2014) 807-811.
[12] J. Chen, H. Zhao, J. He, J. Wang, Si/MgO composite anodes for Li-ion batteries, Rare Met. , 30 (2011) 166-169.
[13] J.M. Yan, H.Z. Huang, J. Zhang, Y. Yang, The study of Mg_2Si/carbon composites as anode materials for lithium ion batteries, J. Power Sources, 175 (2008) 547-552.
[14] H.Kim, J. Choi, H-J.Sohn, T. Kang, The Insertion Mechanism of Lithium into Mg_2Si Anode Material for Li-Ion Batteries, J. Electrochem. Soc., 146 (1999) 4401-4405.

[15] T. Moriga, K. Watanabe, D. Tsuji, S. Massaki, I. Nakabayashi, Reaction Mechanism of Metal Silicide Mg2Si for Li Insertion, J. Solid State Chem., 153 (2000) 386-390.
[16] U. Kasavajjula, C. Wang, A.J. Appleby, Nano- and bulk-silicon-based insertion anodes for lithium-ion secondary cells, J. Power Sources, 163 (2007) 1003-1039.
[17] G. A. Roberts, E. J. Cairns, J. A. Reimer, Mechanism of Lithium Insertion into Magnesium Silicide, J. Electrochem. Soc., 151 (2004) A493.
[18] P. Franke, D. Neuschütz, Mg-Si, in: P. Franke, D. Neuschütz (Eds.) Binary systems. Part 3: Binary Systems from Cs-K to Mg-Zr: Phase Diagrams, Phase Transition Data, Integral and Partial Quantities of Alloys, Springer Berlin Heidelberg, Berlin, Heidelberg, 2005, pp. 1-3.
[19] H. Li, L.Shi, W. Lu, X.Huang, L. Chenz, Studies on Capacity Loss and Capacity Fading of Nanosized SnSb Alloy Anode for Li-Ion Batteries, J. Electrochem. Soc., 148 (2001) A915-A922.
[20] A.C.Larson, R.B.V. Dreele, General Structure Analysis System (GSAS), Los Alamos National Laboratory Report LAUR, (2004) 86-748.
[21] B.H.Toby, EXPGUI, a graphical user interface for GSAS., J.Appl.Crystallogr., 34 (2001) 210-213.
[22] R. Chen, Y-F. Shi, Q -Y. Xu, B-C. Liu, Effect of cooling rate on solidification parameters and microstructure of Al-7Si-0.3Mg-0.15Fe alloy, Trans. Nonferrous Met. Soc. China, 24 (2014) 1645-1652.
[23] C.L. Xu, Q.C. Jiang, Morphologies of primary silicon in hypereutectic Al–Si alloys with melt overheating temperature and cooling rate, Mater. Sci. Eng., A, 437 (2006) 451-455.
[24] C.K. Chan, R. Ruffo, S.S. Hong, Y. Cui, Surface chemistry and morphology of the solid electrolyte interphase on silicon nanowire lithium-ion battery anodes, J. Power Sources, 189 (2009) 1132-1140.
[25] T. Swamy, Y.-M. Chiang, Electrochemical Charge Transfer Reaction Kinetics at the Silicon-Liquid Electrolyte Interface, J. Electrochem. Soc., 162 (2015) A7129-A7134.
[26] C. Xu, F. Lindgren, B. Philippe, M. Gorgoi, F. Björefors, K. Edström, T. Gustafsson, Improved Performance of the Silicon Anode for Li-Ion Batteries: Understanding the Surface Modification Mechanism of Fluoroethylene Carbonate as an Effective Electrolyte Additive, Chem. Mater., 27 (2015) 2591-2599.
[27] Z. Shia, M. Liu, D. Naik, J.L. Gole, Electrochemical properties of Li-Mg alloy electrodes for lithium batteries, J.Power Sources, 92 (2001).
[28] J. Li, J.R. Dahn, An In Situ X-Ray Diffraction Study of the Reaction of Li with Crystalline Si, Journal of The Electrochemical Society, 154 (2007) A156.
[29] K. Ogata, E. Salager, C.J. Kerr, A.E. Fraser, C. Ducati, A.J. Morris, S. Hofmann, C.P. Grey, Revealing lithium-silicide phase transformations in nano-structured silicon-based lithium ion batteries via in situ NMR spectroscopy, Nat Commun, 5 (2014) 3217.
[30] V. Etacheri, O. Haik, Y. Goffer, G.A. Roberts, I.C. Stefan, R. Fasching, D. Aurbach, Effect of fluoroethylene carbonate (FEC) on the performance and surface chemistry of Si-nanowire Li-ion battery anodes, Langmuir, 28 (2012) 965-976.
[31] R. Mogi, M. Inaba, S.-K. Jeong, Y. Iriyama, T. Abe, Z. Ogumi, Effects of Some Organic Additives on Lithium Deposition in Propylene Carbonate, J. Electrochem. Soc., 149 (2002) A1578-A1583.
[32] S.S. Zhang, A review on electrolyte additives for lithium-ion batteries, J.Power Sources, 162 (2006) 1379-1394.
[33] S-W. Song, K.A. Striebel, X. Song, E.J. Cairns, Amorphous and nanocrystalline Mg_2Si thin-film electrodes, J.Power Sources, 119–121 (2003) 110-112.

[34] S-W. Song, K.A. Striebel, R.P. Reade, G.A. Roberts, E.J. Cairns, Electrochemical Studies of Nanoncrystalline Mg_2Si Thin Film Electrodes Prepared by Pulsed Laser Deposition, J. Electrochem. Soc., 150 (2003) A121.
[35] A. Kohandehghan, P. Kalisvaart, M. Kupsta, B. Zahiri, B.S. Amirkhiz, Z. Li, E.L. Memarzadeh, L.A. Bendersky, D. Mitlin, Magnesium and magnesium-silicide coated silicon nanowire composite anodes for lithium-ion batteries, J. Mater. Chem. A, 1 (2013) 1600-1612.
[36] R. Ma, Y. Liu, Y. Yang, M. Gao, H. Pan, Mg_2Si anode for Li-ion batteries: Linking structural change to fast capacity fading, Appl. Phys. Lett., 105 (2014) 213901.
[37] M. Green, E. Fielder, B. Scrosati, M. Wachtler, J.S. Moreno, Structured Silicon Anodes for Lithium Battery Applications, Electrochem. Solid-State Lett., 6 (2003) A75.
[38] H.A. Kramers, Zur Struktur der Multiplett-S-Zustände in zweiatomigen Molekülen. I, Z. Physik., 53 (1929) 422-428.
[39] M. U-Macdonald, S. Real, D.D. Macdonald, Application of Kramers-Kronig Transforms in the Analysis of Electrochemical Impedance Data.II. Transformations in the Complex Plane, J. Electrochem. Soc., 133 (1986).
[40] R.de L. Kronig, J. Opt. Soc. Am., 12 (1926) 547.
[41] BioLogic Science Instruments, EC-Lab software user's manual, 10.1x (2011).
[42] V. Pavlyuk, G. Dmytriv, I. Chumak, O. Gutfleisch, I. Lindemann, H. Ehrenberg, High hydrogen content super-lightweight intermetallics from the Li–Mg–Si system, Int. J. Hydrogen Energy, 38 (2013) 5724-5737.
[43] D. Kevorkov, R. Schmid-Fetzer, F. Zhang, Phase Equilibria and Thermodynamics of the Mg-Si-Li System and Remodeling of the Mg-Si System, J. Phase Equilib. Diffus., 25 (2004) 140-151.
[44] V. Pavlyuk, O.I.Bodak, G.S. Dmytriv, Interaction of components in the Li-(Mg,Al)-Si Systems, Ukr. Khim. Zh. , 58 (1992) 735-737.
[45] S. Wengert, R. Nesper, W. Andreoni, M. Parrinello, Ionic Diffusion in a Ternary Superionic Conductor- An Ab Initio Molecular Dynamics Study, Phys. Rev. Lett., 77 (1996) 5083-5085.
[46] J.F. Herbst, M.S. Meyer, Structural, electronic, and hydriding properties of Li_2MgSi, J. Alloys Compd., 492 (2010) 65-68.

Figure captions in the paper

NANOSTRUCTURED MAGNESIUM SILICIDE Mg2Si

AND IT'S ELECTROCHEMICAL PERFORMANCE

AS AN ANODE OF A LITHIUM ION BATTERY

by

Nazia S. Nazer, Roman V. Denys , Hanne F. Andersen, Lars Arnberg,

and Volodymyr A. Yartys

Figure 1. Phase diagram of Mg-Si [18]. The alloys marked by red cycles are (1) Intermetallic compound Mg_2Si ($Mg_{67}Si_{33}$) and (2) Si-rich eutectic $Mg_{47}Si_{53}$ (Mg_2Si+Si) and were used in this study.

Figure 2. Thermal desorption traces of (a) $2MgH_2$ + Si and (b) $47MgH_2$ + 53Si.

Figure 3. Rietveld refinements of the XRD pattern of (a) Mg_2Si; (b) Mg_2Si +Si, synthesized by HDR method.

Figure 4. SEM images of Mg-Si alloy ; (a) as cast Mg_2Si; (b) RS Mg_2Si ; (c) as cast Mg_2Si+Si ;(d) RS Mg_2Si+Si.

Figure 5. Voltage profiles for (a) Mg_2Si and (b) Mg_2Si+Si electrodes at C/20 rate for the samples synthesized by different routes including (i) HDR; (ii) as-cast and (iii) RS alloys. The data were measured in 1M $LiPF_6$ electrolyte containing EC/PC/DMC (1:1:3)+VC (1 wt.%)+FEC (5wt.%).

Figure 6. Differential capacity plots for the RS Mg_2Si+Si alloy cycled at 0.05C;(a) anodic part; (b) cathodic part. Measurements were performed in 1M $LiPF_6$ in EC/PC/DMC (1:1:3)+VC (1 wt.%)+FEC (5 wt.%) electrolyte.

Figure 7. Nyquist plots of Mg_2Si (a) and Mg_2Si +Si (b) electrodes measured in electrolyte without VC and FEC additives measured using Potentiostatic Electrochemical Impedance Spectroscopy (PEIS) technique along with the fitted data after performing different number of cycles at 100 % DOD. E_{WE} = 0 V vs. E_{oc}; V_a = 10 mV; f_{min} = 40 mHz; f_{max} = 400 kHz with 10 points per decade. Bode plots for Mg_2Si and Mg_2Si +Si electrodes; Magnitude (c) and Phase (d).

Figure 8. Rietveld refinement of the XRD pattern of a fully lithiated Mg_2Si+Si electrode. Bragg peaks positions for the contributing phases are shown (from top to bottom) for Cu, Fe, Mg_2Si, Si, Li_xMg and Li_2MgSi. Inset plot shows the peak at 2θ=31.6º (210), the only observed peak of Li_2MgSi not overlapping with Mg_2Si.

Figure 9. Schematic diagrams of phase transformations for the eutectic electrode on lithiation (a) and for the Mg_2Si electrode on de-lithiation (b). The diagrams show schematically the progression of various steps during galvanostatic tests at C/20. The left scheme assumes presence of four lithiation processes taking place for the Mg_2Si+Si eutectic alloy. The mechanism of the discharge for the stoichiometric Mg_2Si alloy is presented on the right and assumes three de-lithiation events.

Figure 10. Crystal structures of Mg_2Si and its lithiated derivatives $LiMg_2Si$ and Li_2MgSi.